Progress in Reaction Kinetics and Mechanism

ARTICLE

Open Access

https://doi.org/10.48130/prkm-0026-0005

Progress in Reaction Kinetics and Mechanism **2026**, 51: e010

Development of cobalt-based perovskite catalysts for hydrogen production via ammonia decomposition

Cheng Tung Chong[1*], Haoyu Zhang[1], Brandon Han Hoe Goh[1], Shehzad Ahmed[1], Ali R Jalili[2], Agustin Valera-Medina[3], Huijin Xu[4] and Tibor Ajtai[5,6]

[1] *China-UK Low Carbon College, Shanghai Jiao Tong University, Lingang, Shanghai 201306, China*
[2] *School of Chemistry, University of New South Wales (UNSW), Sydney, New South Wales 2052, Australia*
[3] *College of Physical Sciences and Engineering, Cardiff University, Cardiff CF24 3AA, UK*
[4] *School of Merchant Marine, Shanghai Maritime University, Shanghai 201306, China*
[5] *Department of Optics and Quantum Electronics, University of Szeged, Dóm ter 9, Szeged H-6720, Hungary*
[6] *HUN-REN-SZTE Research Group for Photoacoustic Monitoring of Environmental Processes, Dóm ter 9, Szeged 6720, Hungary*
* Correspondence: ctchong@sjtu.edu.cn (Chong CT)

Abstract

The high cost associated with hydrogen storage and transportation pose a significant barrier to the widespread adoption of hydrogen energy. Utilising ammonia as a hydrogen carrier offers a promising solution but the development of an efficient catalyst is critical in reducing the costs of the process. In the present work, a new $La_{(1-x)}Sr_xCoO_3$ (x = 0, 0.2, 0.4, 0.6, 0.8) perovskite composite catalyst was synthesised via the sol-gel method for ammonia decomposition. The effect of the strontium (Sr) doping in the perovskite on ammonia's thermal decomposition was examined. The results show that Sr^{2+} doping can effectively enhance the catalytic activity of the catalyst, in which $La_{0.4}Sr_{0.6}CoO_3$ catalysts exhibited the highest catalytic activity at 650 °C with a decomposition rate of 98.89% and a gas hourly space velocity of 37,500 $mL{\cdot}h^{-1}{\cdot}g^{-1}$. Density functional theory calculation reveals that the $La_{0.4}Sr_{0.6}CoO_3$ exhibits a unique balance of structural, electronic and catalytic properties that optimises NH_3 cracking performance with favourable N_2 desorption characteristics. The enhanced redox activity from the optimal Co^{4+} concentration in $La_{0.4}Sr_{0.6}CoO_3$ reduces the rate-limiting N-H cleavage barrier.

Citation: Chong CT, Zhang H, Goh BHH, Ahmed S, Jalili AR, et al. 2026. Development of cobalt-based perovskite catalysts for hydrogen production via ammonia decomposition. *Progress in Reaction Kinetics and Mechanism* 51: e010 https://doi.org/10.48130/prkm-0026-0005

Introduction

Hydrogen energy is recognised as an important, long-term clean energy option for achieving carbon neutrality. Its use, however, is constrained by high flammability, a strong tendency for leakage, and embrittlement risks in distribution pipelines[1]. Storage and transportation remain challenging and expensive, restricting widespread implementation. Using ammonia (NH_3) as a hydrogen carrier addresses these constraints: it contains ~17 wt% hydrogen, can be stored under near ambient conditions (~7.5 atm, 300 K), and is handled using the already established infrastructure[2]. Ammonia is transported and stored as the carrier and cracked on-site to supply hydrogen. The endothermic cracking of ammonia ($2\ NH_3 \rightarrow N_2 + 3H_2$) provides a clean conversion pathway and a consistent hydrogen stream[3]. In addition, ammonia cracking can feed hydrogen to marine internal combustion engines for propulsion[4] and supply gaseous hydrogen to gas turbines for electricity generation[5]. Nevertheless, the cost and energy efficiency of current cracking systems remain limiting factors, underscoring the need for more effective catalysts[6].

The study of heterogeneous catalysts for ammonia cracking is extensive and encompasses both noble and base metals. The most extensively researched monometallic catalyst for ammonia decomposition is ruthenium (Ru)[6]. Its high intrinsic activity places Ru near the top of the volcano plot for optimal nitrogen binding. The dominant sites on Ru are the B5 ensembles, 3 Ru atoms on a (001) plane with two adjacent step atoms on a (101) plane, maximised on nanoparticles of ~2 nm[7]. This particle size is stabilised by an appropriate metal–support pairing, which maintains favourable kinetics[7]. Representative formulations, 4%Ru–5.4%Ba–7.9%Cs/Sibunit and 4%Ru–13.6%Cs/Sibunit, show high reactivity between 350 and 470 °C for both ammonia decomposition and reverse synthesis[8]. Beyond metal catalysts, compound-mediated routes using nitrogen-rich solids (imides, amides) can also decompose ammonia efficiently; however, their air instability and handling hazards limit their practical use[9]. Consequently, most development has focused on supported metal systems, where activity and durability are tuned through alloying, particle size control, surface basicity and engineered metal–support interactions[10].

On alumina, $Ni/Al_{0.5}Ce_{0.5}O_x$ shows high activity with the lowest reported activation energy; Ce strengthens metal–support interactions, improves stability and promotes B5-like ensembles while facilitating removal of H_2 from the surface[11]. Strong basicity donates electron density to adjust N binding at active sites and accelerate decomposition, resulting in a 25 wt% Ni on lanthanum hexaaluminate catalyst, achieving 85.75% NH_3 conversion at 600 °C and 30,000 $mL{\cdot}g_{cat}^{-1}{\cdot}h^{-1}$[12]. There is a general correlation: increased surface basicity is associated with more robust ammonia decomposition[13]. For instance, 30Fe/SiC-700 with a high basicity that was hydrothermally synthesised achieves a conversion rate of 90.16%[13]. A self-assembled Fe–Co/Al–CeZr catalyst achieves complete decomposition at 550 °C and 6,000 $mL{\cdot}g^{-1}{\cdot}h^{-1}$. The multi-shelled hollow M_xO_y nanosphere structure provides excellent stability and sintering resistance[14]. Strengthening the metal–support interaction is similarly effective: in Ru/Co–Al hydrotalcite, co-precipitation increases the density of oxygen vacancies density, lowers the cracking temperature and achieves 98.57% conversion at 500 °C[15].

Among the non-noble candidates, nickel is widely studied for ammonia decomposition. With appropriate supports and promoters, it can deliver high conversion[16–18]. The availability of Ni

© The Author(s)

adsorption sites is increased, and dehydrogenation steps are facilitated by the higher density of acidic sites, resulting in ~72% conversion from a urine matrix with Ni/Ce-doped Al_2O_3[16]. Dopants with valences that differ from Al^{3+}, such as Sr^{2+}, Zr^{4+} and Ce^{4+}, can significantly increase Ni activity on alumina[16]. Alkaline earth promoters like Ba, Sr, Ca and Mg increase the basicity and electron density around Ni on ceria. This facilitates the recombination and desorption of nitrogen, reducing hydrogen inhibition in the decomposition sequence[17]. Density functional theory supports these trends: Ni/$BaZrO_3$ is predicted to have an overall barrier of ~0.90 eV, with Ni assisting N–H scission and supporting oxygen vacancies, further promoting the pathway[18]. Together, these findings emphasise the importance of catalyst platforms that maintain dispersion at elevated temperatures, regulate hydrogen inhibition and offer tunable basicity and vacancy populations in operating feeds[16–18].

These observations inevitably direct attention to catalyst platforms that maintain dispersion in hot H_2 and NH_3 conditions while simultaneously providing deliberate control over the basicity, reducibility and vacancy chemistry. ABO_3 perovskites offer this combination. By using lower amounts of materials, they can release metal nanoparticles that stay intact and can be restored through redox reactions[19]. Through A site, B site and anion design, including oxynitrides such as hexagonal $BaTiO_{3-x}N_y$, they enable vacancy and basicity control that reduces the operating temperature and maintains activity in moist environments[20].

In this context, Co-based perovskites are attractive for NH_3 cracking because of their ceramic stability, composition flexibility and cost, and because they can be programmed under working feeds to form anchored metal on basic oxides[19]. At the same time, anion-engineered perovskites, including oxynitrides, offer vacancy-rich supports that facilitate lower-temperature operation and enhanced moisture tolerance[20]. Prominent candidates for Co-based perovskites include $LaNiO_3$ and $LaCoO_3$[21]. La is an example of a rare-earth element that can reduce dependence on precious metals while maintaining high reactivity. The barrier for ammonia's dissociation is reduced when La is near Ni(111) according to surface calculations[22]. In direct comparisons, $LaNiO_3$ frequently outperforms $LaCoO_3$ because of the higher surface area and greater reducibility of Ni species[21]. Further performance optimisation can be achieved through adjusting the composition and alloying. For instance, the incorporation of Ce into LaCeNiO improves lower-temperature activity by increasing the surface area, enabling greater reducibility and guaranteeing that the basicity is appropriately set[21]. A perovskite approach can also conserve precious metals, as shown by the fact that alumina-supported $LaFe_{0.9}Ru_{0.1}O_3$ achieves > 99% conversion at 500 °C while using less Ru than a traditional alumina-supported bimetallic Fe–Ru catalyst[23].

Within the perovskite family, activity trends become clear when exsolved metals and support cations are varied. A Co-based single-metal exsolution catalyst delivers 63.9% NH_3 conversion with an H_2 production rate of 21.4 mmol·g_{cat}^{-1}·min^{-1} at 30,000 mL·g_{cat}^{-1}·h^{-1} and 700 °C, outperforming Ni, Fe, NiFe, NiCo and CoFe variants on similar perovskite scaffolds[24]. For cobalt on alkaline earth cerate perovskites, the activity follows the trend 5Co–BaCeO > 5Co–SrCeO > 5Co–CaCeO > 5Co–MgCeO, underscoring the role of the support cation in basicity and metal–support interaction[25]. Oxynitride supports further shift performance, with Ni-loaded perovskite oxynitrides showing 2.5–18× the activity of Ni on oxides; lattice nitrogen and vacancy sites assist activation of ammonia rather than relying solely on the Ni surface[9].

In practice, the performance of mesostructured $LaNiO_3$ is improved by the combination of textural templating and programmed exsolution. This is because the specific surface area is increased and the conversion rate reaches 89% at 550 °C and 30,000 mL·g_{cat}^{-1}·h^{-1} when the mesostructured $LaNiO_3$ is prepared with an SBA-15 template, followed by the exsolution of finely dispersed Ni[26]. An A-site-deficient $Sr_{0.9}Ti_{0.8}Ni_{0.1}Co_{0.1}O_{3-d}$ exsolves 8–12 nm NiCo nanoparticles and outperforms Ni/$SrTiO_3$ and Ni–Co/$SrTiO_3$ benchmarks[27]. Perovskite concepts extend beyond purely thermal routes: titanate-based $Fe_xNi_{1-x}TiO_3$ shows sensitivity to visible light for the conversion of aqueous ammonia under liquid plasma, giving an H_2 production rate of ~140 L·g^{-1}·h^{-1}[28]. Self-combustion-derived $La_{0.1}Ce_{0.9}NiO_3$ and $La_{0.1}Mg_{0.9}NiO_3$ achieve 96% and 98% conversion, respectively, near 400 °C, with stable operation over 40 hours, attributed to their low Ni crystallite size and high basicity. This illustrates how perovskite catalysts can substitute for more expensive Ru systems in accessible temperature windows[29].

We investigated $La_{(1-x)}Sr_xCoO_3$ perovskite catalyst for NH_3 decomposition. Sr, an alkaline earth element, was introduced at the A site to tune vacancy concentration, lattice reducibility and basicity. Prior studies on $La_{(1-x)}Sr_xCoO_3$ reported that increasing the Sr content increases the fraction of Co^{4+} and enhances the lattice's reducibility[30–32]. In our study, Sr was therefore used to adjust the reducibility and the vacancy population, which we probed through temperature-programmed measurements and related the observed activity to the density functional theory (DFT) analysis of vacancy-mediated steps. $La_{(1-x)}Sr_xCoO_3$ was prepared by a sol-gel route across a controlled series with x = 0, 0.2, 0.4, 0.6 or 0.8. Our approach involves the integration of temperature-programmed methods, steady state testing at a fixed gas hourly space velocity, and structural and surface characterisation to quantify performance. The correlations between the catalytic behaviour and the support characteristics, such as vacancy density, basicity and reducibility, were analysed. To quantify the impact of Sr-induced vacancy chemistry on the adsorption energies, dehydrogenation barriers and nitrogen association pathways, DFT mapped elementary steps on representative $La_{(1-x)}Sr_xCoO_3$ surfaces. This was achieved while maintaining the ABO_3 framework as the structural platform.

Materials and methods

Preparation of the perovskite catalyst

$La_{1-x}Sr_xCoO_3$ perovskite at different compositions (x = 0, 0.2, 0.4, 0.6, 0.8) were prepared via the sol-gel technique for the decomposition of NH_3. Analytical grade lanthanum nitrate hexahydrate ($La(NO_3)_3$•$6H_2O$), strontium nitrate ($Sr(NO_3)_2$), cobalt nitrate hexahydrate ($Co(NO_3)_2$•$6H_2O$) and citric acid were used for the synthesis of the perovskites. Each perovskite was prepared by dissolving a set amount of nitrate salt in 50 mL of deionised water before stirring in 0.961 g of citric acid to prepare a 0.1 mol·L^{-1} precursor solution. This mixture was heated to 80 °C while being stirred at 450 rpm for 2 h to form a viscous wet gel, which was then dried in an oven at 120 °C for 12 h. The dried gel was then calcined at 650 °C in a static air atmosphere for 3.5 h. To ensure the safe decomposition of citric acid, the calcination was initiated at 200 °C and held for 15 min before ramping to 650 °C at a heating rate of 10 °C·min^{-1}. After cooling, the calcined perovskite was ground to fine powder form with a ceramic mortar.

Characterisation of the catalyst

X-ray diffraction (XRD) of the perovskite catalyst was conducted using a multifunctional powder X-ray diffractometer (Xpert Powder) from PANalytical. All possible diffraction directions of the lattice

were obtained by scanning the sample within the 2θ angle range, while all the stages were identified through the use of the power diffraction file (PDF) reference database. The morphological structure and elemental composition of the perovskites were analysed via scanning electron microscopy (SEM) (Gemini 300 instrument, ZEISS) paired with energy-dispersive X-ray spectroscopy (EDS) using an INCAx-act detector (Oxford Instruments). Brunauer–Emmett–Teller (BET) analysis was performed to evaluate the specific surface area and pore distribution of the perovskites by using a gas adsorption instrument from Quadrasorb SI by Quantachrome Instruments. Carbon dioxide temperature-programmed desorption (CO_2-TPD) was used to evaluate the basic strength and basic site distribution of the perovskites. The desorption of CO_2 was detected by a gas chromatograph (HP5890) with a thermal conductivity detector (TCD), using the Autosorb-iQ-C chemisoption equipment from Quantachrome for testing. The reduction of the active components in the perovskites was investigated with the Autosorb-iQ-C chemisoption from Quantachrome Instruments via hydrogen temperature-programmed reduction (H_2-TPR).

Ammonia decomposition

The perovskite reduction and ammonia decomposition were conducted in a 400-mm-long vertical quartz tube (inner diameter of 5 mm), whereby the perovskite was held at the centre of the tube with quartz wool. The amount of perovskite catalyst used was 0.08 g for all cases. A schematic diagram of the experimental setup is shown in Fig. 1. The H_2, N_2 and NH_3 gas flows were independently controlled with mass flow controllers and connected to the reactor through a four-way connector. The quartz tube was first purged with 50 mL·min^{-1} of N_2 while being heated to 550 °C at a heating rate of 10 °C·min^{-1}. Then H_2 was introduced into the quartz tube at 25 mL·min^{-1} while the N_2 flow rate was reduced to the same flow rate (H_2 : N_2 = 1:1). The gas flow rate, with a space velocity of 37,500 mL·h^{-1}·g^{-1}, was maintained at 550 °C for 1 h. After the reduction was complete, the H_2 supply was cut off and the perovskite catalyst was cooled to 300 °C in an N_2 flow.

The decomposition of ammonia was evaluated at a temperature range of 300–650 °C. NH_3 was first introduced into the quartz tube at a flow rate of 50 mL·min^{-1} while the N_2 valve was turned off to allow 100% NH_3 flow. The product gas was tested at every 50 °C increment by gas chromatography (GC) on a GC9720Plus (Fuli Instruments) equipped with a TCD to determine the hydrogen content. The GC column used in this study was a RubyBond Packed Column (Porapak Q 60-80 mesh ID.2 mm × 2 m). The hydrogen content was recorded once the value had stabilised for 10 min at the set temperature. Each point of measurement was repeated thrice to obtain an average value. The determined hydrogen content in the gas chromatograph was used to derive the ammonia conversion rate via Eq. (1).

$$\text{Conversion of } NH_3\,(\%) = \frac{H_{2out}}{0.75} \times 100\% \quad (1)$$

Density functional theory calculation

The DFT calculation was performed using the Vienna *ab initio* simulation package (VASP version 5.4.4)[33] to evaluate the mechanism of NH_3 decomposition. The electron exchange–correlation interactions were treated via the generalised gradient approximation (GGA) using the Perdew–Burke–Ernzerhof (PBE) functional[34–37]. To properly describe the strongly correlated 3d electrons of cobalt, the DFT + U approach was used, with an effective U parameter of 3.9 eV for Co 3d orbitals, which accurately reproduced the electronic structure of $LaCoO_3$ perovskites[38]. The projector augmented wave (PAW) method was used to represent the interaction between valence electrons and ionic cores. The plane-wave energy cutoff was set to 500 eV, and structural optimisation was considered to have converged when the total energy changes fell below 1 × 10^{-4} eV and the forces on all the atoms were less than 0.03 eV·Å^{-1}. For the $La_{0.4}Sr_{0.6}CoO_3$ (001) surface, a 25 Å vacuum layer was constructed to eliminate periodic interactions. The Brillouin zone was sampled using a 3 × 3 × 1 Γ-centred k-point mesh for geometric optimisation and a 5 × 5 × 1 mesh for calculating the electronic structure. The adsorption energy (E_{Ads}) of NH_x species was calculated as follows:

$$E_{Ads} = E_{(NH_x/surface)} - \left[E_{surface} + E_{(NH_x)}\right] \quad (2)$$

where, $E_{(NH_x/surface)}$ is the total energy of the adsorbed system, $E_{(surface)}$ is the clean surface energy and $E_{(NH_x)}$ is the energy of the free adsorbate[39]. More negative E_{Ads} values indicate stronger adsorption. The reaction energy barriers (ΔE_a) are determined as follows:

$$\Delta E_a = E(TS) - E(IS) \quad (3)$$

where, *E(TS)* and *E(IS)* are the transition state and initial state energies, respectively. Microkinetic analysis is performed using transition state theory (TST). The rate constant (*k*) for each elementary step is calculated as follows:

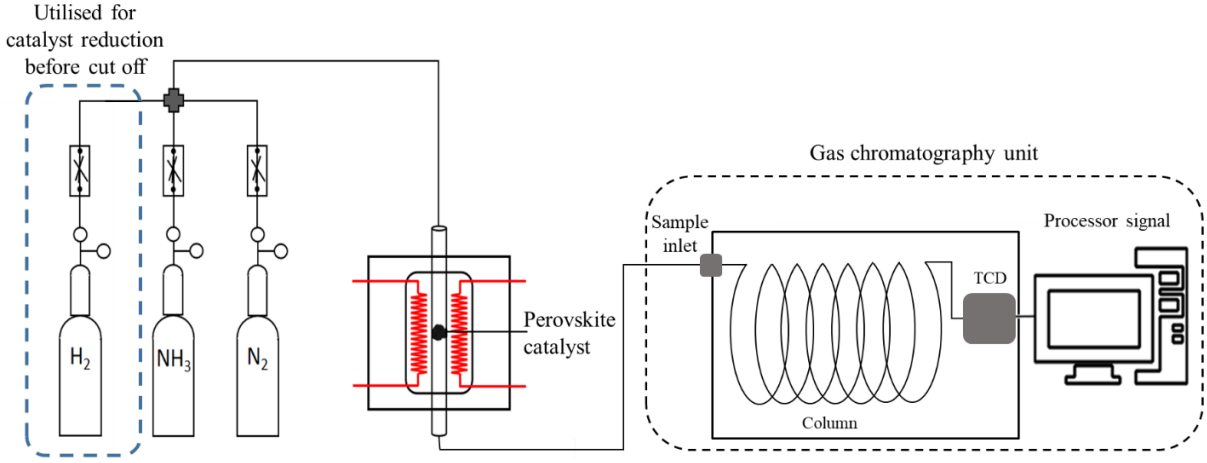

Fig. 1 Schematic of the experimental device for ammonia decomposition.

$$k = (k_B T/h)\, exp(-\Delta G_a/k_B T) \quad (4)$$

where, k_B is Boltzmann's constant, T is the temperature, h is Planck's constant and ΔG_a is the Gibbs free energy of activation[40]. This approach allows an evaluation of temperature-dependent reaction rates and identification of the rate-limiting steps in the NH_3 decomposition mechanism.

Results and discussion

Characterisation of the $La_{(1-x)}Sr_xCoO_3$ catalyst

The XRD characterisation of $La_{(1-x)}Sr_xCoO_3$ (x = 0, 0.2, 0.4, 0.6, 0.8) across the diffraction angle range of 5°–90° is shown in Fig. 2. The $LaCoO_3$ sample shows characteristic peaks at diffraction angles of 23.15°, 32.93°, 33.05°, 40.66°, 47.35° and 58.91°, consistent with the PDF standard card (PDF# 48-0123) for $LaCoO_3$, indicating the high crystallinity of $LaCoO_3$ synthesised via the sol-gel method. The XRD results of $La_{(1-x)}Sr_xCoO_3$ (x = 0.2, 0.4, 0.6, 0.8) showed that characteristic peaks appeared at diffraction angles of 23.145°, 32.97°, 33.044°, 47.373° and 58.835°, consistent with the PDF standard card (PDF# 48-0122) for $La_{0.5}Sr_{0.5}CoO_{2.91}$. In addition, the Sr-doped samples also showed characteristic peaks at 25.11°, 25.79° and 36.56°, which is consistent with the PDF standard card (PDF# 99-0099) for $SrCO_3$. Moreover, the doping of Sr^{2+} also results in various valence states of CoO_x. The XRD results showed the presence of cobalt oxides in the form of CoO and Co_3O_4. As the Sr^{2+} doping increased, the content of the perovskite phase decreased, while the area of the $SrCO_3$ and CoO_x phases increased. Both the perovskite and CoO_x phases contain the Co element, which is the active component for ammonia decomposition. On the other hand, the $SrCO_3$ phase has no obvious catalytic effect. As an impurity phase, the content of $SrCO_3$ gradually increases with the doping of Sr^{2+}. Unlike the CoO_x phase, the $SrCO_3$ phase does not contain active components, and hence the generation of the $SrCO_3$ phase could reduce the crystallinity of the perovskite structure.

The SEM and EDS images of $La_{(1-x)}Sr_xCoO_3$ (x = 0, 0.2, 0.4, 0.6, 0.8) perovskites at different magnifications are shown in Fig. 3. The ionic radius of Sr^{2+} (1.26 Å) is larger than that of La^{3+} (1.061 Å), and hence Sr^{2+} doping could potentially increase the oxidation state of cobalt (Co^{4+}), leading to more oxygen vacancies. When the Sr^{2+} doping ratio increases to 0.8, the particle size of the perovskite becomes larger, which is presumed to be the $SrCO_3$ phase. According to the EDS elemental mapping, as the Sr^{2+} doping ratio increases from 0.2 to 0.6, the elemental distribution of Sr starts to appear on the surface while the La gradually decreases, with the Co element being evenly mixed. However, for the $La_{0.2}Sr_{0.8}CoO_3$, despite some patches of Sr detected on the surface, more O elements are evident, which could be caused by the migration of O atoms to the perovskite's surface. However, images of the individual elemental distribution on the perovskite's surface clearly show the presence of Sr in $La_{0.2}Sr_{0.8}CoO_3$, as evident in Fig. 4q–t. Compared with the baseline $LaCoO_3$ shown in Fig. 4a–d, no element of Sr is observed on the surface. As the doping of Sr increases, an increasing distribution of Sr can be observed, implying that the Sr elements are well dispersed on the catalyst's surface. A notable decrease in the La concentration is observed as the doping ratio of Sr^{2+} increases from 0.4 to 0.6, which is mainly attributed to the decrease in the mass fraction of the perovskite phase. The specific surface area (SSA) measured for the $La_{0.4}Sr_{0.6}CoO_3$ is 38.05 $m^2 \cdot g^{-1}$, and the pore volume and average pore diameter are 0.063 $cm^3 \cdot g^{-1}$ and 3.32 nm, respectively, indicating the mesoporous structure of the catalyst. The SSA is slightly larger than the $LaCoO_3$ catalyst reported in another study[41], which could range across 3.5–13.4 $m^2 \cdot g^{-1}$, depending on the calcination temperature.

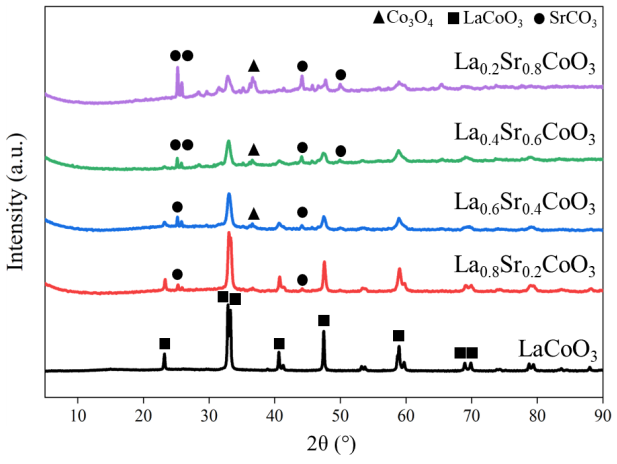

Fig. 2 X-ray diffraction pattern of $La_{(1-x)}Sr_xCoO_3$ perovskite.

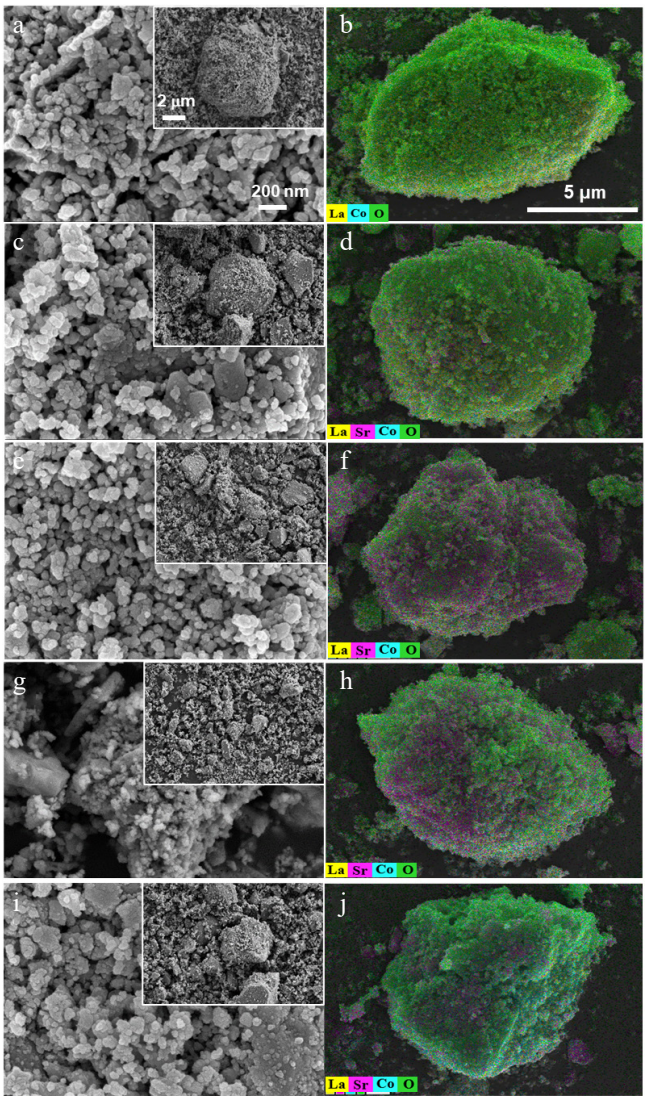

Fig. 3 SEM (first column) and EDS images (second column) of (a), (b) $LaCoO_3$, (c), (d) $La_{0.8}Sr_{0.2}CoO_3$, (e), (f) $La_{0.6}Sr_{0.4}CoO_3$, (g), (h) $La_{0.4}Sr_{0.6}CoO_3$ and (i), (j) $La_{0.2}Sr_{0.8}CoO_3$.

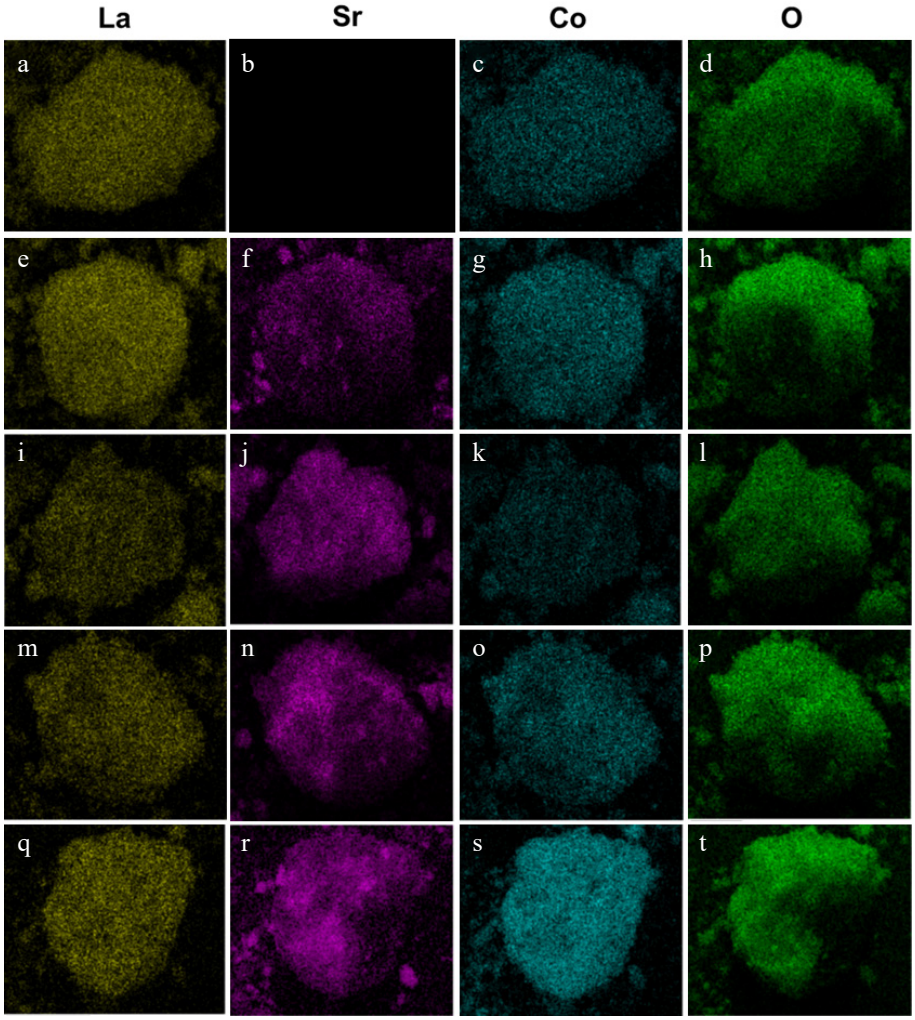

Fig. 4 Elemental distribution of La, Sr, Co and O for (a)–(d) $LaCoO_3$, (e)–(h) $La_{0.8}Sr_{0.2}CoO_3$, (i)–(l) $La_{0.6}Sr_{0.4}CoO_3$, (m)–(p) $La_{0.4}Sr_{0.6}CoO_3$ and (q)–(t) $La_{0.2}Sr_{0.8}CoO_3$.

The H_2-TPR curves of the $La_{(1-x)}Sr_xCoO_3$ catalysts are shown in Fig. 5a. For the $LaCoO_3$ catalyst, there is an obvious TCD low-temperature peak (340 °C) and a TCD overlap peak in the temperature range of 400–750 °C, with the maximum peak appearing at 540 °C. The low-temperature peak is related to the reduction of unstable lattice oxygen in the $LaCoO_3$ crystal, whereas the TCD overlap peak is the subsequent reduction of $Co^{3+} \rightarrow Co^{2+}$ and $Co^{2+} \rightarrow Co^{0}$[42], which can defined as follows:

$$LaCoO_3 + \frac{1}{2}H_2 \rightarrow LaCoO_{2.5} + \frac{1}{2}H_2O \quad (5)$$

$$LaCoO_{2.5} + H_2 \rightarrow \frac{1}{2}La_2O_3 + Co + H_2O \quad (6)$$

From Fig. 5a, it can also be seen that doping with Sr^{2+} causes the TCD peaks to shift to a lower temperature, suggesting that doping promotes the Co reduction process in the perovskite. As the Sr doping increases from x = 0.6 to 0.8, the peaks shift to a higher temperature, indicating that beyond this point, excessive doping of Sr^{2+} reduces the perovskite's reducibility. Excessive Sr^{2+} doping leads to a significant production of the $SrCO_3$ impurity phase which is difficult to reduce. In the TCD peak area, it is noticed that more Sr^{2+} doping increases the TCD peak area, leading to a higher consumption of H_2 for reduction. At the temperature range of 50–200 °C, it is observed that doping with Sr^{2+} increased the consumption of hydrogen at low temperatures, which may be caused by Sr^{2+} causing oxygen to adsorb on the catalyst's near-surface region after the reduction treatment[43]. However, beyond x = 0.6, the reducibility of the $La_{(1-x)}Sr_xCoO_3$ catalyst reduces, thereby inhibiting the ammonia cracking activity.

The basicity of a catalyst plays a key role in the desorption of nitrogen atoms, which is the rate-determining step during ammonia cracking[41]. Alkaline earth elements are known to effectively improve the catalytic activity of perovskite catalysts by increasing the basicity of the catalysts[44]. The CO_2-TPD method was used to measure the basicity of each perovskite, as shown in Fig. 5b. Each perovskite displays peaks in the low-temperature region (100–250 °C) and the medium-temperature region (250–500 °C), which represent weak and medium alkaline sites, respectively[45]. There is a slight shift to higher temperatures as Sr^{2+} doping increases from 0 to 0.6, indicating that Sr^{2+} doping enhances the alkalinity of the perovskite. For the low-temperature TCD signal, the peak area first decreases then increases as the Sr^{2+} doping increases from x = 0 to 0.6. There is a marked increase in the low-temperature peak area when Sr^{2+} doping is at x = 0.8, as a large amount of $SrCO_3$ disrupts the perovskite's structure (as shown by the increase in the CoO_x phase) and converts some of the medium basic sites into weak basic sites. This is also noticeable for the medium-temperature TCD peak areas (an initial increase followed by a decrease), where the number of medium-basic sites decreases at Sr^{2+} doping at x = 0.8.

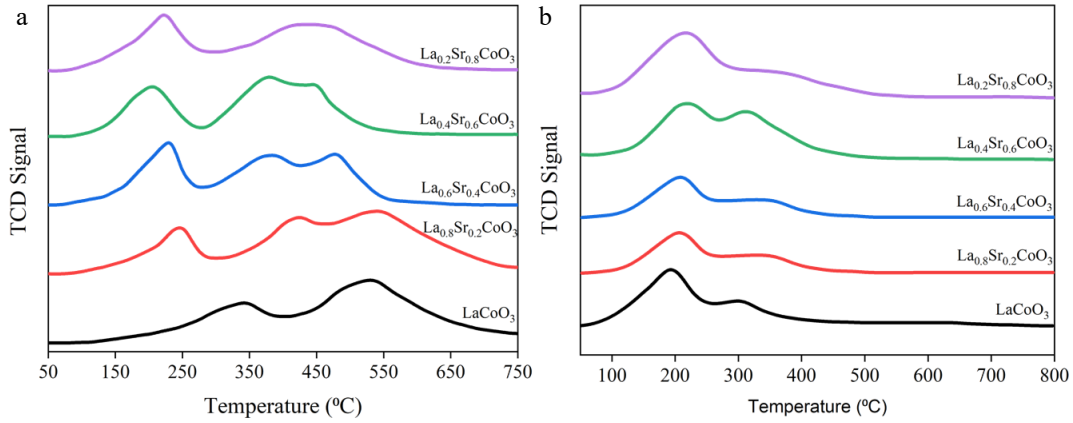

Fig. 5 (a) H_2-TPR curve and (b) CO_2-TPD image of $La_{(1-x)}Sr_xCoO_3$ perovskites.

These findings highlight the importance of an appropriate amount of Sr^{2+} doping to optimise the reducibility and increase the number of medium-basic sites, which are important properties that lead to an increase in ammonia decomposition activity. From the characterisation results, a Sr^{2+} doping rate of x = 0.6 shows the optimal reducibility with highest number of medium-basic sites present in the perovskite, suggesting the composition is most optimal for ammonia decomposition.

Catalytic ammonia decomposition performance

Ammonia decomposition is an endothermic reaction[46]. Full decomposition of NH_3 can occur at relatively high temperatures, often requiring the catalyst to keep the reaction stable at temperatures beyond 600 °C[18]. In the present test, each $La_{(1-x)}Sr_xCoO_3$ perovskite was evaluated for its effect on ammonia decomposition from 300 to 650 °C, as shown in Fig. 6. At 600 °C, the order of catalytic activity for ammonia decomposition decreased as follows: $La_{0.4}Sr_{0.6}CoO_3$ > $La_{0.6}Sr_{0.4}CoO_3$ > $La_{0.8}Sr_{0.2}CoO_3$ > $LaCoO_3$ > $La_{0.2}Sr_{0.8}CoO_3$. It is evident that Sr doping significantly increased the rate of ammonia decomposition up to the level of x = 0.6 before decreasing again at x = 0.8. $La_{0.4}Sr_{0.6}CoO_3$ shows the highest catalytic activity with 91.92% conversion at 600 °C and nearly complete conversion at 650 °C. During the thermal decomposition of NH_3, a series of reactions happen via the mechanism shown in Eqs (7)–(12):

$$NH_3 \rightleftharpoons NH_{3,ad} \quad (7)$$

$$NH_{3,ad} \rightleftharpoons NH_{2,ad} + H_{ad} \quad (8)$$

$$NH_{2,ad} + H_{ad} \rightleftharpoons NH_{ad} + 2H_{ad} \quad (9)$$

$$NH_{3,ad} + 2H_{ad} \rightleftharpoons N_{ad} + 3H_{ad} \quad (10)$$

$$2H_{ad} \rightleftharpoons H_2 \quad (11)$$

$$2N_{ad} \rightleftharpoons N_2 \quad (12)$$

The N recombination reaction (Eq. [12]) is the key determinant reaction that determines the rate of the reaction. If the binding energy of the N-N bond formation is not achieved, this will hinder the formation of N_2, thereby slowing down the rate of ammonia decomposition. Ammonia decomposition mainly occurs at the basic sites on the perovskite's surface[47]. When the Sr^{2+} doping ratio is at 0.6, the TCD peak in the medium-temperature zone appears at the high-temperature zone with the largest area, indicating that $La_{0.4}Sr_{0.6}CoO_3$ has higher basicity with more basic sites. The rate-determining step for ammonia decomposition is dependent on the type of catalyst and the operating conditions, which can be

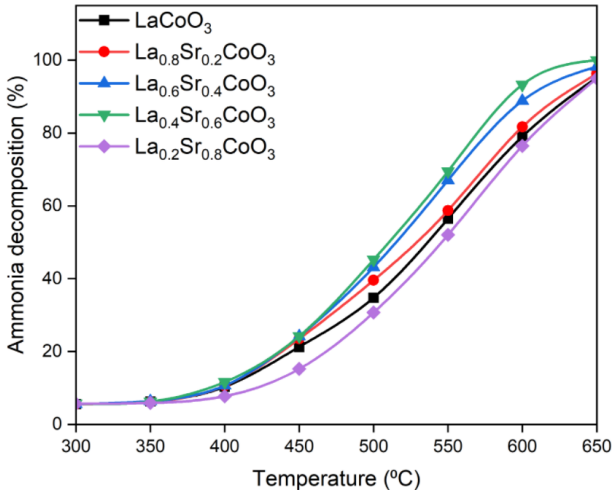

Fig. 6 Ammonia decomposition performance of $La_{(1-x)}Sr_xCoO_3$ perovskite between 300–650 °C.

enhanced by selecting suitable supports, adjusting the appropriate temperature and gas composition and by optimising the catalyst's surface structure and active sites[48]. Figure 6 shows that the $La_{0.4}Sr_{0.6}CoO_3$ catalyst achieved the highest conversion at 650 °C, which is attributable to the high basicity induced by the basic sites. This agrees with a previous study which concluded that a catalyst with higher surface basicity tends to possess stronger ability to decompose NH_3[13]. In the case where Sr^{2+} doping is at 0.8, the alkalinity of the catalyst is significantly lower, which results in a lower ammonia conversion rate.

Test of the catalyst's stability and performance comparison

A continuous 12-h ammonia cracking test was conducted using the $La_{0.4}Sr_{0.6}CoO_3$ catalyst to examine its stability performance. The experiment was performed at 550 °C at a constant flow rate and cracking temperature. The hydrogen content produced by thermal catalytic cracking was measured each hour to obtain the ammonia conversion rate. Figure 7 shows the result of the 12-h ammonia cracking conversion rate for the $La_{0.4}Sr_{0.6}CoO_3$ catalyst. Throughout the test, the catalyst remained stable with a consistent conversion rate of 68%–70%. Despite the slight fluctuation, no significant deviation was observed, suggesting resistance to sintering and thermal deactivation during the test period. Note, however, that the test was conducted only for 12 h, whereas the stability of the

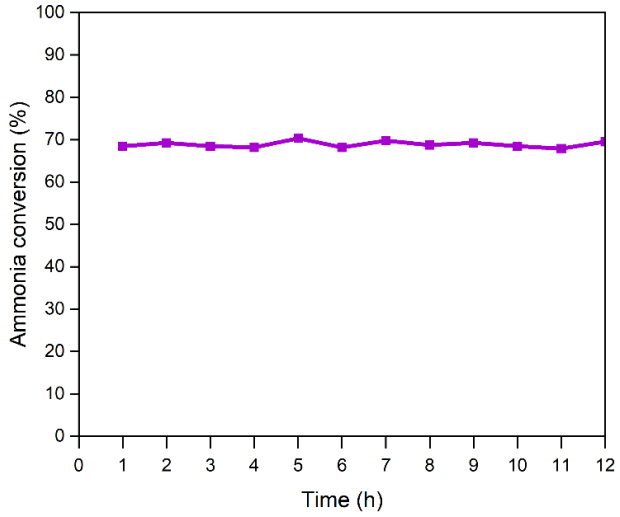

Fig. 7 Ammonia conversion rate of the $La_{0.4}Sr_{0.6}CoO_3$ catalyst during the ammonia catalytic decomposition reaction.

catalyst for longer periods will require more in-depth tests to ensure its robustness and durability for industrial use.

Table 1 shows the performance of the newly developed perovskite-based catalyst ($La_{0.4}Sr_{0.6}CoO_3$) compared with other thermal catalysts. Under reaction conditions of 500 °C and a gas hourly space velocity (GHSV) of 37,500 $mL{\cdot}h^{-1}{\cdot}g^{-1}$, the ammonia conversion rate of the present $La_{0.4}Sr_{0.6}CoO_3$ catalyst is 43.2%, which is higher than the single-metal Co/γ-Al_2O_3 (21%) and Mo/γ-Al_2O_3 (22.4%) catalysts under a similar GHSV of 36,000 $mL{\cdot}h^{-1}{\cdot}g^{-1}$ at 500 °C[49]. However, for the γ-alumina supported Co–Mo catalyst, the ammonia conversion rate is 55% at the same temperature and GHSV, indicating the enhanced catalytic performance of the bimetallic catalyst[49]. Xie et al.[50] developed high-entropy alloy (HEA) catalysts comprising $Co_xMo_yFe_{10}Ni_{10}Cu_{10}$ (x + y = 70) for ammonia decomposition, and reported that HEA-$Co_{45}Mo_{25}$ exhibited a conversion rate of 64.5% at 500 °C. The nitrogen-doped carbon nanotube (CNT)-supported noble metal (Ru) catalyst shows an ammonia conversion rate of 48% at 400 °C, albeit with a diluted mixture of NH_3-He (1:2.4) and a GHSV of 6,000 $mL{\cdot}g^{-1}{\cdot}h^{-1}$[51]. Choudhary et al.[52] demonstrated that Ru/SiO_2 can achieve an ammonia conversion rate of 64% at 500 °C. When Ni/SiO_2 was doped with La, the performance was higher than that of the present $La_{0.4}Sr_{0.6}CoO_3$ catalyst, but Ce doping resulted in a slightly lower ammonia conversion rate[53]. Strong catalytic performance was demonstrated by MnN-$LiNH_2$ with a 75.2% conversion rate achieved at 465 °C, which is about twice as high as that of MnN-$NaNH_2$ (32.0%) at the same temperature, indicating the strong promoting effect of the former alkali metal amides[54]. Nevertheless, the stability and the reactive performance of the present perovskite-based catalyst make it a prospective catalyst for thermal decomposition of ammonia.

DFT calculations

The high thermal stability of perovskite oxides makes them suitable for the catalytic decomposition of NH_3 into N_2 and H_2[18]. Figure 8a summarizes the proposed NH_3 decomposition pathway on the $La_{(1-x)}Sr_xCoO_3$ catalyst's surface. As shown in Fig. 8b, at a low Sr^{2+} substitution rate of $x \leq 0.6$, the lattice contracts, consistent with the $Co^{3+} \rightarrow Co^{4+}$ oxidation that shortens the Co–O bond's length, whereas the b-axis remains nearly constant (~7.122 Å). Beyond x = 0.6, the volume expands, and the b-axis exhibits a maximum near x = 0.8, revealing a competing structural response such as octahedral tilting/orbital ordering. Overall, these trends reflect strong charge–lattice coupling, with a composition of x = ~0.6 providing a particularly favourable balance between structural distortion and the Co oxidation state. This balance correlates with improved NH_3 cracking performance, potentially aided by enhanced redox flexibility and lattice-oxygen participation associated with changes in the Co^{3+}/Co^{4+} ratio, which can accelerate surface reaction cycles.

The adsorption energies of NH_x intermediates (NH_3, NH_2, NH* and N*) systematically weaken as the Sr content increases up to x = 0.6 (Fig. 8b, c). Specifically, the NH_3* adsorption energy drops from –0.64 eV at x = 0 to –0.39 eV at x = 0.6, whereas N* binding weakens from –3.09 to –2.10 eV, representing an overall decrease of approximately 32%–35% in the adsorption strength. This pattern aligns with $Co^{3+} \rightarrow Co^{4+}$ oxidation, which reduces electron density at the active Co sites and consequently diminishes the binding strength of nitrogen-containing intermediates. Significantly, $La_{0.4}Sr_{0.6}CoO_3$ reaches a balanced adsorption state, as shown in Fig. 8d, where NH_2* (–0.92 eV) and NH* (–1.38 eV) are stabilised enough to facilitate the activation of NH_3, yet not so strongly bound as to cause surface poisoning. The atomic structure for each model catalyst used in the DFT calculation is shown in the supplementary material (Supplementary Fig. S1).

As shown in Fig. 9a, decomposition of NH_3 on $La_{0.4}Sr_{0.6}CoO_3$ occurs through sequential dehydrogenation steps, $NH_3^* \rightarrow NH_2^* + H^* \rightarrow NH^* + 2H^* \rightarrow N^* + 3H^*$, with transition state barriers of 0.42, 1.10 and 1.54 eV, respectively (these energies are referenced to the preceding adsorbed state). The highest barrier is for the final N–H cleavage step (1.54 eV), which is lower than that reported for

Table 1. Performance of different catalysts in thermal catalytic decomposition of NH_3.

Catalyst	Metallic loading (wt %)	GHSV ($mL{\cdot}g^{-1}{\cdot}h^{-1}$)	Reaction temperature (°C)	Ammonia conversion rate (%)	Ref.
Ru/N-CNT	7	6,000	400	48.0	[51]
Ru/SiO_2	10	30,000	500	64.0	[52]
Co/γ–Al_2O_3	5	36,000	500	21.0	[49]
Mo/ γ–Al_2O_3	5	36,000	500	22.4	[49]
CoMo/ γ–Al_2O_3	5	36,000	500	55.0	[49]
Fe_5Co/CNTs	5	36,000	600	48.0	[55]
*HEA-$Co_{45}Mo_{25}$	8.8	36,000	500	64.5	[50]
Co_7Mo_3/MCM-41	5	36,000	500	51.8	[56]
MnN-$LiNH_2$	49.9	13,500	465	75.2	[54]
MnN-$NaNH_2$	46.7	13,500	465	32.0	[54]
Ni-0.1La/SiO_2	–	30,000	500	46.5	[53]
Ni-0.1Ce/SiO_2	–	30,000	500	40.2	[53]
$La_{0.4}Sr_{0.6}CoO_3$	–	37,500	500	43.2	This work

*HEA, high-entropy alloy.

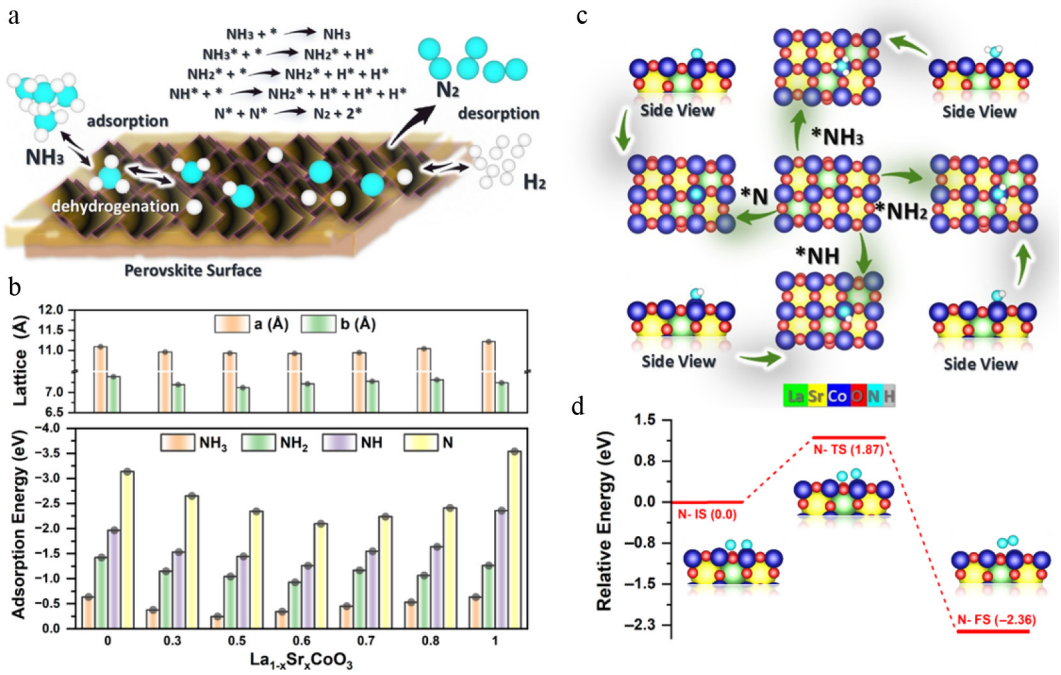

Fig. 8 (a) Pathway of the NH_3 decomposition mechanism, with * denoting active sites. (b) Lattice contraction ($x \leq 0.6$) to expansion ($x > 0.6$) and NH_x adsorption energies (weakest at $x = 0.6$). Inset: NH_3 on Co (1.82 Å). (c) Optimised NH_3/NH_2/NH/N structures. (d) N desorption profile: 1.87 eV barrier, exothermic (−2.36 eV) at $x = 0.6$.

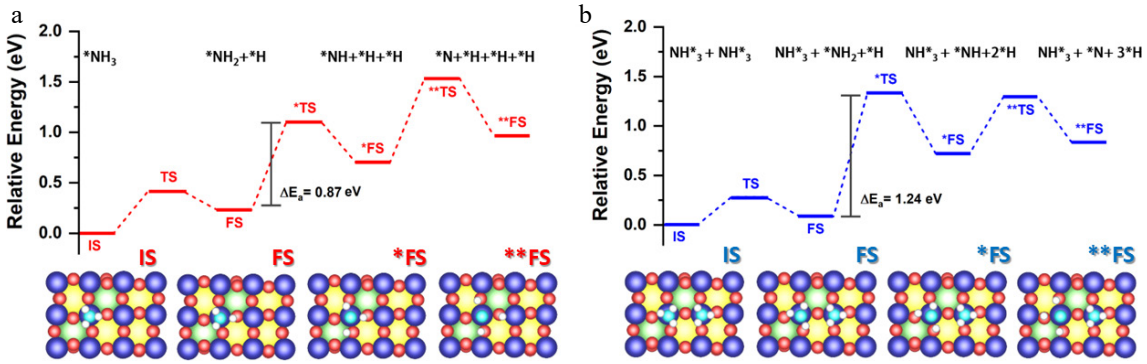

Fig. 9 (a) Mechanism of NH_3 decomposition on $La_{0.4}Sr_{0.6}CoO_3$ perovskite catalysts. Reaction pathway showing sequential dehydrogenation steps (NH_3* → NH_2* → NH* → N*) and N_2 desorption, with energy distributions for key intermediates at different Sr doping levels ($x = 0$–1). (b) Optimised structures (top and side views) illustrating the dimerised decomposition mechanism at the active Co site, with bond lengths of 1.86 Å and relative energies indicated.

$LaCoO_3$ (> 1.8 eV), consistent with the altered electronic structure at $x = 0.6$ (e.g., an increased Co^{4+} fraction). In addition to the monomeric route, Fig. 9b shows a cooperative dimer pathway in which two co-adsorbed NH_3* species undergo stepwise dehydrogenation, (NH_3* + NH_3 → NH_3 + NH_2* + H*) → (NH_3* + NH* + 2H*) → (NH_3* + N* + 3H*), with transition state energies of 0.28, 1.34 and 1.30 eV, respectively. This dimer pathway presents barriers that are similar to or lower than those of the monomer route, as shown in Fig. 9b. It decreases the likelihood of strongly bound N* building up (final-state energy: ~0.82 eV), indicating a more favourable kinetic balance between activation of NH_3 and N_2 formation. Overall, the combined reaction profiles indicate that $La_{0.4}Sr_{0.6}CoO_3$ is the most kinetically advantageous composition among those studied.

$La_{0.4}Sr_{0.6}CoO_3$ outperforms both the Sr-deficient ($x < 0.5$) and Sr-rich ($x > 0.7$) analogues, which may be associated with an improved balance of surface adsorption strength, lattice distortion and redox behavior. However, its NH_3 decomposition activity remains lower than that of precious metal catalysts and alkali metal amide systems, such as MnN-$LiNH_2$[54] and Ru-KNH_2/GNP[57], it should be noted that the present catalyst is expected to achieve even higher ammonia conversion rates at higher weights, hourly space velocities and ammonia concentrations. The $La_{0.4}Sr_{0.6}CoO_3$ represents an optimally engineered perovskite catalyst for efficient NH_3 cracking, achieving the crucial balance between NH_3 activation and nitrogen desorption. Through systematic Sr doping, this composition overcomes the classic trade-off between activity and stability that plagues many transition metal catalysts. Future work should explore the interplay between Co^{4+}/oxygen vacancy ratios and long-term stability under varying reaction conditions.

Conclusions

In the present work, a cobalt-based perovskite doped with Sr was developed for the decomposition of NH_3 to produce hydrogen. Sr doping on the A-site of the perovskite surface enables a strong

metal–support interaction that promote catalytic stability while maintaining the perovskite's structure. The results show that the decomposition rate of NH_3 is enhanced with the use of the catalyst as the temperature increases, among which the $La_{0.4}Sr_{0.6}CoO_3$ catalyst exhibited the highest catalytic activity at 650 °C with a decomposition rate of 98.89% with a NH_3 flow rate of 37,500 mL·h^{-1}·g^{-1}. The high reactivity of $La_{0.4}Sr_{0.6}CoO_3$ is attributable to the high basicity induced by the doping of Sr, which generated more basic sites. The result corroborates the DFT calculation, which showed that Sr doping at a rate of 0.6 exhibits a unique balance of structural, electronic and catalytic properties that optimises the NH_3 cracking performance. This is attributed to the moderate adsorption energy is required for N_2 desorption and the enhanced redox activity from Co^{4+} and oxygen vacancies. In general, the NH_3 decomposition reaction pathway shows a sequential dehydrogenation step of NH_3* → NH_2* → NH* → N*, in which the $La_{0.4}Sr_{0.6}CoO_3$ composition's optimal Co^{4+} concentration reduces the rate-limiting N-H cleavage barrier (1.54 eV) compared with $LaCoO_3$ (> 1.8 eV). Moreover, the $La_{0.4}Sr_{0.6}CoO_3$ perovskite also enables efficient NH_3 cracking via a cooperative dimer mechanism. The lattice contraction of $La_{0.4}Sr_{0.6}CoO_3$ perovskite further stabilises the intermediates, yielding lower barriers than monomeric pathways. Among the Sr-doped catalysts, the $La_{0.4}Sr_{0.6}CoO_3$ strikes an ideal balance among adsorbate binding, lattice dynamics and redox activity, implying that the optimum Sr doping rate for $LaCoO_3$ can enhance the reactivity for decomposing NH_3. This work provides insight into the mechanism of perovskite-based catalysts for efficient hydrogen production via NH_3 cracking.

Author contributions

The authors confirm their contributions to the paper as follows: conceptualization, funding acquisition, supervision: Chong CT; investigation, formal analysis: Zhang H, Goh BHH, Ahmed S; writing – review & editing: Chong CT, Zhang H, Goh BHH, Ahmed S, Jalili AR, Valera-Medina A, Xu H, Ajtai T. All authors reviewed the results and approved the final version of the manuscript.

Data availability

The datasets generated during and/or analyzed during the current study are available from the corresponding author on reasonable request.

Acknowledgments

The authors gratefully acknowledge the funding from the Scientific and Innovative Action Plan of Shanghai, the International Collaboration Research Fund by Science and Technology Commission of Shanghai Municipality (23160712400), the General Program of the National Natural Science Foundation of China (52476122), the Royal Society—National Natural Science Foundation of China (NSFC) International Exchanges Cost Share (W2521172) and the Shanghai Jiao Tong University (SJTU)-University of New South Wales (UNSW) Collaborative Research Program 2025.

Conflict of interest

The authors declare that they have no known competing financial interests or personal relationships that could have appeared to influence the work reported in this paper.

Supplementary information accompanies this paper online at: https://doi.org/10.48130/prkm-0026-0005.

Dates

Received 3 December 2025; Revised 3 January 2026; Accepted 3 February 2026; Published online 7 May 2026

References

[1] Wang S, Chong CT, Józsa V, Chiong MC. 2024. Investigation of NO emissions and chemical reaction kinetics of ammonia/methane flames under dual-fuel co-combustion mode at elevated air temperature conditions. *International Journal of Hydrogen Energy* 84:968–981

[2] Chiong MC, Chong CT, Ng JH, Mashruk S, Chong WWF, et al. 2021. Advancements of combustion technologies in the ammonia-fuelled engines. *Energy Conversion and Management* 244:114460

[3] Ya Y, Xu YS, Elbanna AM, Liu Y, Sun B, et al. 2025. Review of direct ammonia solid oxide fuel cells: low temperature cell structure and ammonia decomposition strategies. *Renewable and Sustainable Energy Reviews* 213:115350

[4] Fan Y, Zhu T, Li Z, Li J, Ren F, et al. 2025. Non-equilibrium plasma cracking assisted ammonia marine engine for zero carbon emissions. *International Journal of Hydrogen Energy* 112:433–445

[5] Richard S, Santos AR, Oliver P, Gallucci F. 2024. Techno-economic analysis of ammonia cracking for large scale power generation. *International Journal of Hydrogen Energy* 71:571–587

[6] Medina E, Fernández C, Karelovic A, Jiménez R. 2024. A review: rational design of catalysts for catalytic decomposition of ammonia. *International Journal of Hydrogen Energy* 90:1435–1466

[7] Zecher-Freeman N, Zong H, Xie P, Wang C. 2023. Catalytic cracking of ammonia toward carbon-neutral liquid fuel. *Current Opinion in Green and Sustainable Chemistry* 44:100860

[8] Shlyapin DA, Borisov VA, Temerev VL, Iost KN, Fedorova ZA, et al. 2023. Ammonia synthesis and decomposition in the presence of supported ruthenium catalysts. *Kinetics and Catalysis* 64(6):815–825

[9] Miyashita K, Ogasawara K, Miyazaki M, Abe H, Niwa Y, et al. 2024. Effects of nitrogen vacancy sites of oxynitride support on the catalytic activity for ammonia decomposition. *NPG Asia Materials* 16:54

[10] Han T, Wei L, Xie S, Liu Y, Dai H, et al. 2025. Catalyst design for ammonia decomposition: an overview. *Industrial Chemistry & Materials* 3:311–331

[11] Yu M, Sun R, Luo G, Wang L, Li X, et al. 2024. Ammonia partial cracking over low-cost Ni catalysts for enhancing combustion. *Fuel* 367:131306

[12] Li G, Yu X, Lei Z, Yin F, Zhang H, et al. 2023. Preparation of lanthanum hexaaluminate supported nickel catalysts for hydrogen production by ammonia decomposition. *Catalysis Letters* 153:3148–3158

[13] Liu Y, Yin F, Li G, Tan Y. 2025. Preparation of silicon carbide supported iron catalysts and their catalytic activities in hydrogen production by ammonia decomposition. *Catalysis Letters* 155:13

[14] Hao S, Ding C, Wang T, Zheng S, Wang Z. 2025. Fe-Co/Al-CeZr-M multi-shelled nanosphere catalysts derived from self-templated synthesis for hydrogen production by ammonia decomposition. *Fuel* 397:135425

[15] Li Z, Guo L, Ren W, Han J, Verma SK, et al. 2024. Hydrogen production from ammonia decomposition over Ru/Co–Al-LDOs catalysts prepared by a one-step synthesis method of co-precipitation. *International Journal of Hydrogen Energy* 9:1000–1010

[16] Henpraserttae S, Charojrochkul S, Lawtrakul L, Toochinda P. 2018. Ni-based catalysts for hydrogen production from ammonia decomposition: effect of dopants and urine application. *Chemistry Select* 3:11842–11850

[17] Zhang Z, Yu M, Shen M, Li W, Shen G. 2025. Promoting effect of alkaline earth metals on Ni/CeO_2 catalysts for ammonia decomposition reaction. *Molecular Catalysis* 578:115016

[18] Qin C, Ruan S, He C, Zhang L. 2024. Nickel perovskite catalysts for ammonia decomposition: DFT calculations and microreaction kinetics. *Colloids and Surfaces A: Physicochemical and Engineering Aspects* 691:133898

[19] Neagu D, Tsekouras G, Miller DN, Ménard H, Irvine JTS. 2013. *In situ* growth of nanoparticles through control of non-stoichiometry. *Nature Chemistry* 5:916–923

[20] Ogasawara K, Miyazaki M, Miyashita K, Abe H, Niwa Y, et al. 2023. Ammonia decomposition over water-durable hexagonal $BaTiO_3$–xNy-supported Ni catalysts. *Advanced Energy Materials* 13(35):2301286

[21] Podila S, Driss H, Ali AM, Al-Zahrani A A, Daous MA. 2022. Influence of Ce substitution in LaMO3 (M = Co/Ni) perovskites for CO_x-free hydrogen production from ammonia decomposition. *Arabian Journal of Chemistry* 15:103547

[22] Usman M, Ali A, Jedidi A, Ajeebi A, Hossain MM, et al. 2025. Rare earth metal promoters (La, Ce, Nd, Sm) on nickel-supported Al_2O_3 catalysts for ammonia decomposition. *Fuel* 396:135272

[23] Jeong JH, Lee S, Kim JY, Kwon BW. 2025. Highly effcient and stable Ru-doped $LaFeO_3$ based perovskite catalyst for green hydrogen production *via* ammonia decomposition. *International Journal of Hydrogen Energy* 126:36–44

[24] Jeong H, Kim YH, Jang W, Ji Y, Hong JE, et al. 2024. *In-situ* prepared co exsolution nano catalyst for efffcient hydrogen generation *via* ammonia decomposition. *Solid State Ionics* 416:116679

[25] Al-attar OA, Podila S, Al-Zahrani AA. 2023. Preparation and study of $XCeO_3$ (X: Mg, Ca, Sr, Ba) perovskite-type oxide supported cobalt catalyst for hydrogen production by ammonia decomposition. *Arabian Journal for Science and Engineering* 48:8667–8677

[26] Gamez S, Romdhane FB, Schnee J, Gaigneaux EM. 2025. Ni-exsolved catalysts from hard templated mesoporous $LaNiO_3$ perovskite for highly effcient NH_3 decomposition. *Chemical Engineering Journal* 506:160377

[27] Ren H, Zhi G, Chen C, Fang H, Lin Z, et al. 2024. *In situ* exsolution of Ni–Co alloys from A-site-deficient perovskite for efficient ammonia decomposition. *International Journal of Hydrogen Energy* 96:385–395

[28] Jung SC, Chung KH. 2024. Enhanced hydrogen production through cracking of ammonia water using liquid plasma on titanate-based perovskite catalysts. *Energy Conversion and Management* 311:118509

[29] Pinzón M, Sánchez-Sánchez A, Romero A, de la Osa AR, Sánchez P. 2022. Self-combustion Ni and co-based perovskites as catalyst precursors for ammonia decomposition. Effect of Ce and Mg doping. *Fuel* 323:124384

[30] Mizusaki J, Mima Y, Yamauchi S, Fueki K, Tagawa H. 1989. Nonstoichiometry of the perovskite-type oxides $La_{1-x}Sr_xCoO_{3-\delta}$. *Journal of Solid State Chemistry* 80(1):102–111

[31] Lankhorst MHR, Bouwmeester HJM, Verweij H. 1997. High-temperature coulometric titration of $La_{1-x}Sr_xCoO_{3-\delta}$: evidence for the effect of electronic band structure on nonstoichiometry behavior. *Journal of Solid State Chemistry* 133(2):555–567

[32] Wang P, Yao L, Wang M, Wu W. 2000. XPS and voltammetric studies on $La_{1-x}Sr_xCoO_{3-\delta}$ perovskite oxide electrodes. *Journal of Alloys and Compounds* 311(1):53–56

[33] Hafner J. 2008. *Ab-initio* simulations of materials using VASP: density-functional theory and beyond. *Journal of Computational Chemistry* 29(13):2044–2078

[34] Zhao Y, Schultz NE, Truhlar DG. 2005. Exchange-correlation functional with broad accuracy for metallic and nonmetallic compounds, kinetics, and noncovalent interactions. *The Journal of Chemical Physics* 123:161103

[35] Mori-Sánchez P, Cohen AJ, Yang W. 2006. Self-interaction-free exchange-correlation functional for thermochemistry and kinetics. *The Journal of Chemical Physics* 124:091102

[36] Perdew JP, Burke K, Ernzerhof M. 1996. Generalized gradient approximation made simple. *Physical Review Letters* 77(18):3865–3868

[37] Ernzerhof M, Scuseria GE. 1999. Assessment of the perdew–burke–ernzerhof exchange-correlation functional. *Journal of Chemical Physics* 110:5029–5036

[38] Himmetoglu B, Floris A, de Gironcoli S, Cococcioni M. 2014. Hubbard-corrected DFT energy functionals: the LDA+U description of correlated systems. *International Journal of Quantum Chemistry* 114(1):14–49

[39] Ahmed S, Muhammad I, Ghani A, Muhammad I, Ullah N, et al. 2024. Two-dimensional ABS_4 (A and B = Zr, Hf, and Ti) as promising anode for Li and Na-Ion batteries. *Molecules* 29(21):5208

[40] Fellmuth B, Gaiser C, Fischer J. 2006. Determination of the Boltzmann constant—status and prospects. *Measurement Science and Technology* 17:R145

[41] Pinzón M, Sánchez-Sánchez A, Sánchez P, de la Osa AR, Romero A. 2021. Ammonia as a carrier for hydrogen production by using lanthanum based perovskites. *Energy Conversion and Management* 246:114681

[42] Onrubia-Calvo JA, Pereda-Ayo B, De-La-Torre U, González-Velasco JR. 2017. Key factors in Sr-doped $LaBO_3$ (B = Co or Mn) perovskites for NO oxidation in efficient diesel exhaust purification. *Applied Catalysis B: Environmental* 213:198–210

[43] Wang X, Huang K, Qian J, Cong Y, Ge C, et al. 2017. Enhanced CO catalytic oxidation by Sr reconstruction on the surface of $La_xSr_{1-x}CoO_{3-\delta}$. *Science Bulletin* 62:658–664

[44] Aihara T, Aoki W, Ishikawa S, Bae S, Kiyohara S, et al. 2025. Significant enhancement of the basicity of $SrTiO_3$ nanoparticles by alkali metal doping: implication for the Knoevenagel condensation. *ACS Applied Nano Materials* 8(32):15988–15998

[45] Wang T, Su M, Wang Q, Li Z. 2023. Effect of Ca on perovskite $La_{1-x}Ca_xNiO_3$ catalyst for CO_2 hydrogenation-to-light hydrocarbons in a dielectric barrier discharge plasma reactor. *Energy Technology* 11(8):2300180

[46] Bell TE, Ménard H, González Carballo JM, Tooze R, Torrente-Murciano L. 2020. Hydrogen production from ammonia decomposition using Co/γ-Al_2O_3 catalysts – insights into the effect of synthetic method. *International Journal of Hydrogen Energy* 45:27210–27220

[47] Gallus S, Weidenthaler C. 2023. Systematic *in situ* investigation of the formation of NH_3 cracking catalysts from precursor perovskites ABO_3 (A=La, Ca, Sr and B=Fe, Co, Ni) and their catalytic performance. *ChemCatChem* 15(21):e202300947

[48] Zhu N, Yang F, Hong Y, Liang J. 2025. Hydrogen production from ammonia decomposition: advances in Ru- and Ni-based catalysts. *International Journal of Hydrogen Energy* 98:1243–1261

[49] Ji J, Duan X, Qian G, Zhou X, Tong G, et al. 2014. Towards an efficient CoMo/γ-Al_2O_3 catalyst using metal amine metallate as an active phase precursor: enhanced hydrogen production by ammonia decomposition. *International Journal of Hydrogen Energy* 39(24):12490–12498

[50] Xie P, Yao Y, Huang Z, Liu Z, Zhang J, et al. 2019. Highly efficient decomposition of ammonia using high-entropy alloy catalysts. *Nature Communications* 10:4011

[51] Bell TE, Zhan G, Wu K, Zeng HC, Torrente-Murciano L. 2017. Modification of ammonia decomposition activity of ruthenium nanoparticles by N-doping of CNT supports. *Topics in Catalysis* 60:1251–1259

[52] Choudhary TV, Sivadinarayana C, Goodman DW. 2001. Catalytic ammonia decomposition: COx-free hydrogen production for fuel cell applications. *Catalysis Letters* 72(3–4):197–201

[53] Yao L, Shi T, Li Y, Zhao J, Ji W, et al. 2011. Core–shell structured nickel and ruthenium nanoparticles: very active and stable catalysts for the generation of CO_x-free hydrogen *via* ammonia decomposition. *Catalysis Today* 164(1):112–118

[54] Chang F, Guo J, Wu G, Wang P, Yu P, et al. 2017. Influence of alkali metal amides on the catalytic activity of manganese nitride for ammonia decomposition. *Catalysis Today* 286:141–146

[55] Zhang J, Müller JO, Zheng W, Wang D, Su D, et al. 2008. Individual Fe–Co alloy nanoparticles on carbon nanotubes: structural and catalytic properties. *Nano Letters* 8(9):2738–2743

[56] Duan X, Qian G, Zhou X, Chen D, Yuan W. 2012. MCM-41 supported Co single bond Co–Mo bimetallic catalysts for enhanced hydrogen production by ammonia decomposition. *Chemical Engineering Journal* 207–208:103–108

[57] Chang F, Wu H, van der Pluijm R, Guo J, Ngene P, et al. 2019. Effect of pore confinement of $NaNH_2$ and KNH_2 on hydrogen generation from ammonia. *The Journal of Physical Chemistry C, Nanomaterials and Interfaces* 123(35):21487–21496

Copyright: © 2026 by the author(s). Published by Maximum Academic Press, Fayetteville, GA. This article is an open access article distributed under Creative Commons Attribution License (CC BY 4.0), visit https://creativecommons.org/licenses/by/4.0/.